Revisiting the Magnetic Field of the L183 Starless Core

Janik Karoly^{1,2}, Archana Soam², B-G Andersson², Simon Coudé², Pierre Bastien³, John E. Vaillancourt⁴, and Chang Won Lee^{5,6}

Department of Physics, Santa Clara University, Santa Clara, 500 El Camino Real, Santa Clara, CA, USA; jkaroly@alumni.scu.edu
 SOFIA Science Center, Universities Space Research Association, NASA Ames Research Center, M.S. N232-12, Moffett Field, CA 94035, USA; asoam@usra.edu
 Institut de Recherche sur les Exoplanètes (iREx) & Centre de Recherche en Astrophysique du Québec (CRAQ), Université de Montréal, Département de Physique, C.P. 6128 Succ. Centre-ville, Montréal, QC, H3C 3J7, Canada

⁴ Lincoln Laboratory, Massachusetts Institute of Technology, 244 Wood Street, Lexington, MA 02420-9108, USA
 ⁵ Korea Astronomy & Space Science Institute, 776 Daedeokdae-ro, Yuseong-gu, Daejeon, Republic of Korea
 ⁶ University of Science and Technology, Korea, 217 Gajeong-ro, Yuseong-gu, Daejeon 34113, Republic of Korea
 Received 2020 April 27; revised 2020 August 4; accepted 2020 August 5; published 2020 September 15

Abstract

We present observations of linear polarization from dust thermal emission at 850 μ m toward the starless cloud L183. These data were obtained at the James Clerk Maxwell Telescope (JCMT) using the SCUBA-2 camera in conjunction with its polarimeter POL-2. Polarized dust emission traces the plane-of-sky magnetic field structure in the cloud, thus allowing us to investigate the role of magnetic fields in the formation and evolution of its starless core. To interpret these measurements, we first calculate the dust temperature and column density in L183 by fitting the spectral energy distribution obtained by combining data from the JCMT and the Herschel space observatory. We used the Davis–Chandrasekhar–Fermi technique to measure the magnetic field strength in five subregions of the cloud, and we find values ranging from \sim 120 \pm 18 μ G to \sim 270 \pm 64 μ G in agreement with previous studies. Combined with an average hydrogen column density ($N_{\rm H_2}$) of \sim 1.5 \times 10²² cm⁻² in the cloud, we also find that all five subregions are magnetically subcritical. These results indicate that the magnetic field in L183 is sufficiently strong to oppose the gravitational collapse of the cloud.

Unified Astronomy Thesaurus concepts: Interstellar medium (847); Starlight polarization (1571); Magnetic fields (994)

1. Introduction

In the current paradigm of star formation, the filamentary structures found in molecular clouds are expected to fragment into dense cores of dust and gas (with hydrogen volume densities of $n_{\rm H_2} > 10^4 \, {\rm cm}^{-3}$) as a necessary step before stars can be formed through gravitational collapse. Indeed, farinfrared and submillimeter observations in the past two decades have shown that these dense cores are ubiquitous in nearby star-forming regions (e.g., André et al. 2014). However, not all cores are observed to harbor a protostar (e.g., di Francesco et al. 2007). These "starless" cores are typically divided into two categories: (1) unbound cores supported against gravity by thermal pressure, which, along with gravitationally bound cores such as B86 (Alves et al. 2001), can be modeled as Bonnor-Ebert spheres (Ebert 1955; Bonnor 1956), and (2) collapsing prestellar cores transitioning into first hydrostatic cores' (e.g., Machida et al. 2008).

The L183 cloud (Lynds 1962, aka L134N), and its starless cores (Spitzer image shown in Figure 1), is an ideal candidate to study the role of magnetic fields at the onset of star formation, and specifically to probe if they can moderate the gravitational collapse of prestellar cores. Indeed, at a distance of 110 pc (Franco 1989), the proximity and low Galactic longitude (l=6.1) of L183 means it is a cloud with a significant number of background stars despite its high Galactic latitude (b=36.8) (Pagani et al. 2003).

Lee et al. (1999, 2001, 2004) listed L183 as a possible infall candidate based on spectroscopic measurements of the

CS (2-1), CS (3-2), N_2H^+ (1-0), and DCO $^+$ (2-1) molecular lines. The L183 core has a $C^{18}O$ depletion level typically associated with chemically evolved cores (Tafalla 2005a, 2005b), yet it shows no signs of hosting embedded young stellar objects even though less-evolved cores like L1521F are already undergoing star formation (Tafalla 2005a, 2005b; A. Soam et al. 2020, in preparation). It is therefore possible that the gravitational collapse of L183 is significantly curtailed either because of the gas kinematics or the magnetic energy inside the core.

In this work, we investigate the contribution of the magnetic field to the stability of L183. This is achieved by using $850~\mu m$ observations obtained with the POL-2 polarimeter at the James Clerk Maxwell Telescope (JCMT). The structure of magnetic fields in the interstellar medium can be directly inferred from the polarization of dust thermal emission at far-infrared and submillimeter wavelengths (see Andersson et al. 2015, and references therein). Such emission polarization is expected to be perpendicular to the plane-of-the-sky field orientation due to the alignment of interstellar dust grains with magnetic fields through radiative alignment torques. The alignment efficiency of dust grains in the dense environment of L183 will be investigated in a forthcoming paper (B.-G. Andersson & A. Soam et al. 2020, in preparation).

Assuming a distance of 110 pc, our 850 μ m observations achieve a spatial resolution of 7.5 mpc (or 1600 au) while simultaneously mapping all of the highest extinction regions in the cores over a \sim 12′ wide field (see Figures 1 and 2). Crutcher et al. (2004) also observed L183 at a comparable resolution using the SCUPOL polarimeter (the predecessor of POL-2) at the JCMT, but they were limited to a much smaller \sim 3.5′ wide region with a lower sensitivity than our POL-2 data (see Section 3.7). Nevertheless, their original analysis suggested

These objects represent an early phase in the low-mass star formation process, after collapse of the parent core has begun but before a true protostar has formed.

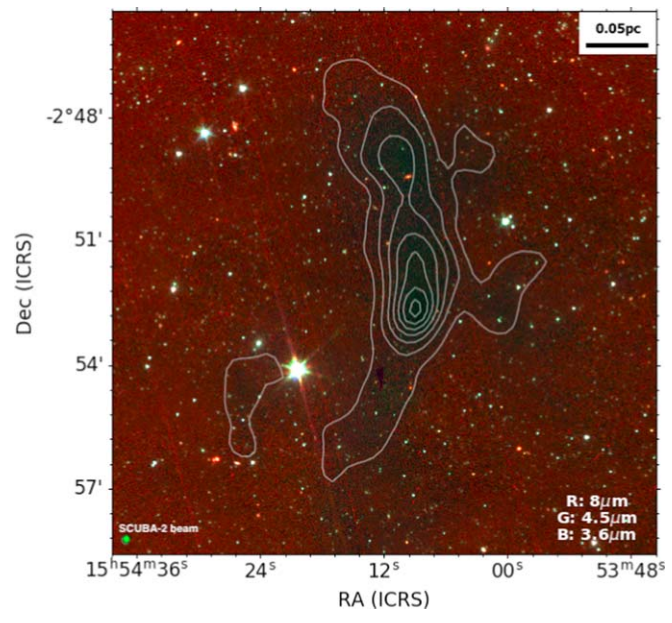


Figure 1. Combined Spitzer observations of L183 taken with IRAC at 8, 4.5, and 3.6 μ m. The contours trace the 850 μ m dust emission map from SCUBA-2 starting at 10 mJy beam⁻¹ and increasing in increments of 20 mJy beam⁻¹. The green circle in the lower left corner shows the JCMT/SCUBA-2 beam size.

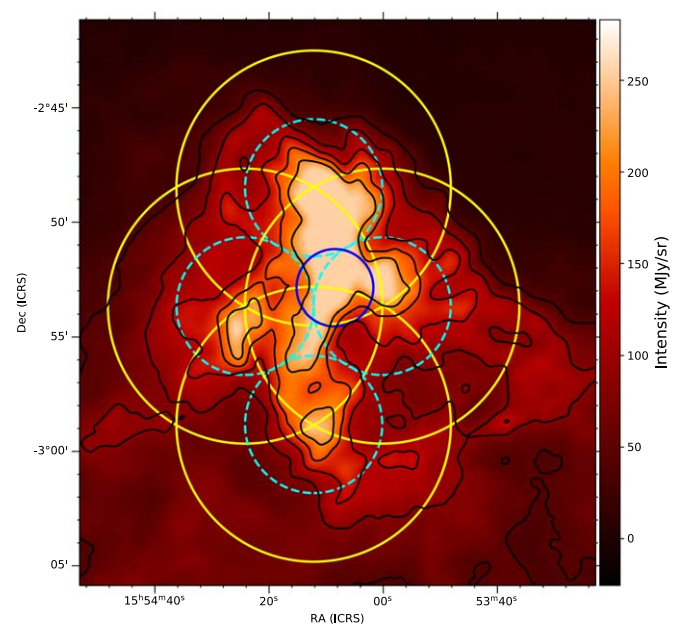


Figure 2. The dust emission toward L183 as traced by Herschel 500 μ m Spectral and Photometric Imaging Receiver (SPIRE) observations. The plain blue circle in the center indicates the limited area previously observed with SCUPOL by Crutcher (2004). The yellow circles indicate the four POL-2 Daisy fields covered in our observations. These field of views are optimized so that their central 6' wide areas (dashed cyan circles), where POL-2's sensitivity is optimal, are centered on high-density regions while still fully covering the main body of the L183 cloud.

that L183 may be only weakly supercritical, i.e., the magnetic energy is at least three times smaller than, and at most equal to, the gravitational energy in the core ($E_{\rm grav}/3 < E_{\rm mag} < E_{\rm grav}$). With the higher sensitivity of POL-2, we significantly improve the accuracy of this criticality measurement.

The POL-2 data presented in this work provide the deepest polarization observations to date of a starless core. Although significant improvements have been made in recent years to the sensitivity of polarimetric instruments, polarimetry at farinfrared and submillimeter wavelengths still presents unique technical challenges (see Pattle & Fissel 2019) that are compounded by the faint polarization signature of starless cores. This low polarized emission is explained by the combination of two main factors: First, the dust content of starless cores is typically colder than in active star-forming regions ($T_d \approx 7 \text{ K}$ for L183, Pagani et al. 2003, see also Section 3.2), thus leading to weaker dust thermal emission. Second, the polarization efficiency in starless cores is known to decrease sharply as a function of visual extinction A_V (e.g., Alves et al. 2014; Jones et al. 2015), which results in a decrease of the degree of polarization in the denser parts of the cloud. Thus, observations to date have been used mostly to study magnetic fields in all but the brightest starless cores. Prior to this work, Crutcher et al. (2004) and Ward-Thompson et al. (2000) have used SCUPOL to study the bright starless cores L183, and L1544 and L43, respectively.

This paper is structured as follows: Section 2 presents the observations and the data reduction process. Section 3 provides a discussion of the main results, such as the dust properties (Section 3.2), the magnetic field morphology (Section 3.3), the field strength (Section 3.4), the criticality criterion (Section 3.5), and the energy budget of the cloud (Section 3.6), as well as a comparison with previous SCUPOL results (Section 3.7). Finally, we summarize the findings of this paper in Section 4.

2. Observations and Data Reduction

The observations were conducted with SCUBA-2/POL-2 at 850 μm in 2019 February and March (M19AP009; PI: Bastien, P.) using the polarimetric Daisy-map mode of the JCMT (Holland et al. 2013; Friberg et al. 2016; P. Bastien et al. 2020, in preparation). The POL-2 polarimeter, which consists of a fixed polarizer and a half-wave plate rotating at a frequency of 2 Hz, is placed in the optical path of the SCUBA-2 camera. Figure 2 shows the locations of the observations on L183 Herschel/ SPIRE image. The weather conditions during observations were split between $au_{225} < 0.05$ and $0.05 < au_{225} < 0.08$, where au_{225} is the atmospheric opacity at 225 GHz. The total integration time for a single field was \sim 4 hr to complete six full Daisy patterns. SCUBA-2/POL-2 simultaneously collects data at 450 and 850 μ m with effective FWHM beam sizes of 9.6" and 14.1", respectively (Dempsey et al. 2013). For this work, we focused exclusively on the 850 μ m data due to the signal-to-noise ratio (S/N) in the 450 μ m data being too low to recover a sufficient number of polarization vectors for the analysis.

We observed four separate subregions (north, south, east, and west) overlapping near the center of the cloud. For the POL-2 Daisy-map mode, a fully sampled circular region of 12' diameter is produced, with a high signal-to-noise coverage over the central 6' wide area. This observing mode is based on the SCUBA-2 constant velocity Daisy scan pattern (Holland et al. 2013), but modified to have a slower scan speed (i.e., 8'' s⁻¹ compared to the original 155'' s⁻¹) to obtain sufficient on-sky data to measure the Stokes Q and U values accurately at every point of the map. The integration time decreases toward the edges of the map, which consequently leads to an increase in the rms noise levels.

To reduce the data, we used the STARLINK/SMURF (Chapin et al. 2013; Currie et al. 2014) package pol2map specifically developed for submillimeter data obtained with the JCMT. The details of the data reduction procedure are presented in Wang et al. (2019), and we will only summarize the relevant steps here.

First, the raw bolometer time streams are converted into Stokes I, Q, and U time streams at a sampling rate of a full half-wave plate rotation through the process calcqu. A Stokes I map is then created from all Stokes I time streams using the routine makemap, which is an iterative map-making process. Individual I maps corresponding to each observation were co-added to produce the initial I map of each region (see Chapin et al. 2013). Because four separate regions were observed to cover the cloud, we co-added the initial Stokes I map from each region to get the complete Stokes I map.

The final Stokes I, Q, and U maps were obtained by running pol2map a second time. The initial Stokes I mosaic map is used to generate a fixed S/N-based mask for all subsequent iterations of makemap. During the final process, we corrected for the loss of synchronization between data values and pointing information in the data reduction process via the skyloop⁸ parameter in pol2map. This parameter improves the recovery of fainter, extended emission in the map by iterating individual observations in parallel. This is in contrast to the traditional JCMT map-making method of deriving an iterative solution for each observation individually. The resulting Stokes I, Q, and U maps for the four separate regions were then co-added to produce the final maps used for this study.

The resulting Stokes I, Q, and U maps were flux calibrated, in units of mJy beam $^{-1}$, using a flux calibration factor for 850 μ m of 725 Jy pW $^{-1}$. The final co-added Stokes I, Q, and U maps have an rms noise 10 of ~ 1.5 mJy beam $^{-1}$. Finally, the data were reduced with a 12" pixel size at each step.

After the final step of running pol2map, we obtain a polarization vector catalog produced from the co-added Stokes I, Q, and U maps. The final polarization values obtained here are debiased using the Stokes Q and U variances to remove the statistical bias in regions of low signal-to-noise ratio (S/N; Wardle & Kronberg 1974).

The values for the debiased degree of polarization P were calculated from

$$P = \frac{1}{I} \sqrt{Q^2 + U^2 - \frac{1}{2} (\delta Q^2 + \delta U^2)},$$
 (1)

where I, Q, and U are the Stokes parameters, and δQ , and δU are the uncertainties for Stokes Q and U (see Soam et al. 2019; Wang et al. 2019). The uncertainty δP of the polarization degree was obtained using

$$\delta P = \sqrt{\frac{(Q^2 \delta Q^2 + U^2 \delta U^2)}{I^2 (Q^2 + U^2)} + \frac{\delta I^2 (Q^2 + U^2)}{I^4}},$$
 (2)

with δI being the uncertainty for the Stokes I total intensity.

The polarization position angles θ , increasing from north to east in the sky projection, were measured using the relation

$$\theta = \frac{1}{2} \tan^{-1} \frac{U}{Q}.\tag{3}$$

The corresponding uncertainties in θ were calculated using

$$\delta\theta = \frac{1}{2} \frac{\sqrt{Q^2 \delta U^2 + U^2 \delta Q^2}}{(Q^2 + U^2)} \times \frac{180^{\circ}}{\pi}.$$
 (4)

The plane-of-sky orientation of the magnetic field is inferred by rotating the polarization angles by 90° (assuming that the polarization is caused by elongated dust grains aligned perpendicular to the magnetic field).

3. Analysis

3.1. Polarization and Magnetic Fields

In our analysis of the POL-2 data, we only use data points where the observed uncertainties in position angle are less than 20°. Additionally, we impose an additional constraint of $I/\delta I > 10$ to improve the reliability of our analysis. We checked the quality of the data used for the analysis by examining different S/N values derived from the polarization intensity (PI) and its uncertainty (δ_{PI}). In Figure 3(a), the magnetic field orientations inferred from S/N > 3 (PI/ $\delta_{PI} > 3$; 124 blue vectors) and S/N > 2 (PI/ δ_{PI} > 2; 236 red vectors [some of the red vectors are hidden under the blue ones]) are generally consistent within the cloud. The goal of this comparison is to evaluate the validity of using the lower S/N threshold of S/N > 2 instead of the stricter S/N > 3. The additional vectors plotted using S/N > 2 have similar polarization percentages and position angles to the S/N > 3 vectors in their vicinity, which suggests that the larger population of S/N > 2 vectors can be used for the analysis. Additionally, in panels (b) and (c) of Figure 3, the distributions of position angles and polarization percentages follow similar behaviors, further justifying our use of the $PI/\delta_{PI} > 2$ values.

Figure 4 shows the morphology of the magnetic field in the inner parts of the L183 cloud. Here, the lengths of the vectors have been normalized for clarity; they do not represent the polarization percentage. Rather than evaluating the magnetic field structure of L183 by using a single structure function, we instead chose to split the cloud into five regions with distinct populations of magnetic field lines based on their apparent uniformity in polarization angle (see Figure 5). This allows us to employ the classical interpretation of the Davis-Chandrasekhar-Fermi method (DCF; Chandrasekhar & Fermi 1953) to derive the magnetic field strength independently for each region. Previous studies of magnetic field strength (e.g., Coudé et al. 2019), use an improved DCF method developed by Houde et al. (2009) and Hildebrand et al. (2009), which uses an angular dispersion function. We used this angular dispersion function on the five regions seen in Figure 5. However, for regions 1-4, the function failed to converge in 200 iterations. In region 5, the calculated turbulent-to-ordered magnetic energy ratio, $\langle B_t^2 \rangle / \langle B_o^2 \rangle$, was 21.93 \pm 46.56 and the reduced chisquared value for the fit of the angular dispersion function was 5.3. The large energy ratio uncertainty gives an indeterminate result. For these observations, the data sets are too noisy and therefore the contribution from turbulence cannot be distinguished from beam smoothing. As a reference, our noise level ($\sim 1.5 \text{ mJy beam}^{-1}$) is comparable to that of SCUBA-2/POL-2

⁸ http://starlink.eao.hawaii.edu/docs/sc22.pdf

This conversion was done using the CALIBRATE-SCUBA-2-DATA recipe under the PICARD package in STARLINK.

 $^{^{10}}$ This value was measured using the SCUBA-2-MAPSTATS recipe under the PICARD package in STARLINK.

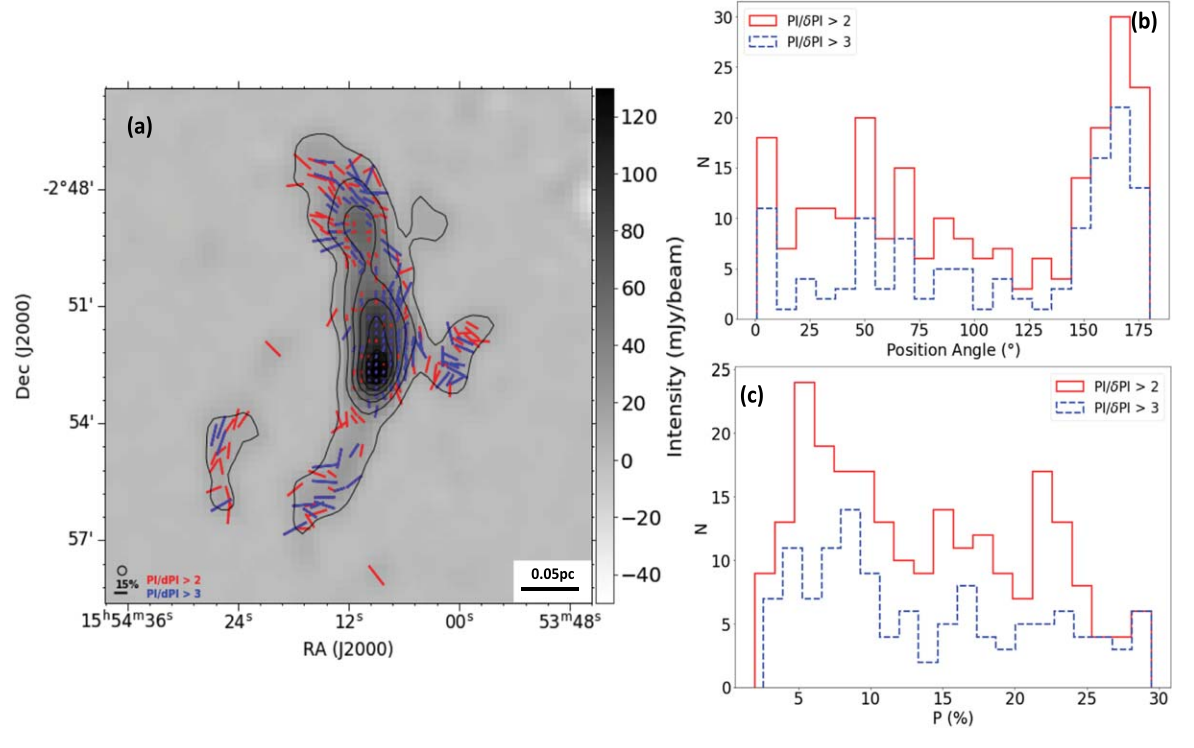


Figure 3. Panel (a) shows the magnetic field orientations in L183 with $PI/\delta PI > 2$ (red vectors) and $PI/\delta PI > 3$ (blue vectors). The vectors are plotted on the 850 μm dust emission map with overlaid contours starting at 10 mJy beam⁻¹ and increasing by 20 mJy beam⁻¹. The JCMT 850 μm beam size and the vector scale are shown in the bottom left corner. Panels (b) and (c) show the distributions of magnetic field position angles and polarization percentages, respectively.

observations of B1 (Coudé et al. 2019) although L183 is approximately three times dimmer. We therefore use the DCF method used in Crutcher et al. (2004) to calculate the magnetic field strength.

Figure 5 shows the five regions and their respective distributions of position angles, including the Gaussian fit for each. The total distribution of position angles shown in Figure 6 appears to follow a double-Gaussian distribution, although the second peak is rather broad. In regions 1, 3, and 4, we have taken advantage of the 180° ambiguity in magnetic field direction (e.g., a vector with position angle of 15° shows the same direction as one with a position angle of 195°) to best demonstrate the Gaussian distributions of the position angles.

The DCF method assumes that the geometry of the magnetic field is uniform in each region, and so measuring the dispersion of position angles allows us to estimate the field strength. This dispersion in position angles is explained by local turbulence disrupting the magnetic field structure. We also assume that the distribution of vectors around the mean field direction is approximately Gaussian, and is therefore well characterized by its standard deviation. The DCF method determines the field strength using the following equation:

$$B_{\rm pos} = Q_c \sqrt{4\pi\rho} \frac{\sigma_v}{\sigma_\theta},\tag{5}$$

where Q_c is a correction factor that accounts for variations of the magnetic field on scales smaller than the beam, ρ is the gas density, σ_v is the one-dimensional nonthermal velocity dispersion of the gas, and σ_θ is the dispersion in polarization angle. Crutcher (2004) further approximated this formulation as

$$B_{\rm pos} \approx 9.3 \sqrt{n(H_2)} \frac{\Delta v}{\sigma_{\theta}} \mu G,$$
 (6)

where Q_c has been taken to be 0.5 (Ostriker et al. 2001), $n(H_2)$ is volume density of molecular hydrogen, and Δv is the FWHM of the gas velocity calculated by $\Delta v = \sigma_v \sqrt{8 \ln 2}$. The units are cm⁻³ for the volume density $n(H_2)$, km s⁻¹ for Δv , and degrees for σ_θ .

3.2. Dust Column Densities and Temperatures

L183 was previously observed by the Herschel space observatory with SPIRE at 250, 350, and 500 μ m, as well as with the Photodetector Array Camera & Spectograph (PACS) at 100 and 160 μ m. We use this archival Herschel data at 160, 250, 350, and 500 μ m, combined with our JCMT data at 850 μ m, to fit a modified blackbody function (see Equation (7)) for the dust emission in L183. The Herschel/PACS, Herschel/SPIRE, and JCMT 850 μ m images were smoothed to the SPIRE 500 μ m FWHM beam size of 35.2" and then reprojected on a common grid.

The spectral energy distribution (SED) for each pixel was fitted assuming the following formula for a modified blackbody emission (see Kauffmann et al. 2008):

$$S_{\nu} = B_{\nu}(T_{\rm d})(1 - e^{-\tau_{\nu}}),$$
 (7)

$$B_{\nu}(T_{\rm d}) = \frac{2h\nu^3}{c^2} \frac{1}{e^{h\nu/k_{\rm B}T_{\rm d}} - 1},\tag{8}$$

$$\tau_{\nu} = \mu_{\rm H_2} m_{\rm H} \kappa_{\nu} N_{\rm H_2},\tag{9}$$

and

$$\kappa_{\nu} = \kappa_o \left(\frac{\nu}{\nu_o}\right)^{\beta},\tag{10}$$

where S_{ν} is the measured flux at the observed frequency ν , $B_{\nu}(T_{\rm d})$ is the Planck function for a dust temperature $T_{\rm d}$, τ_{ν} is the

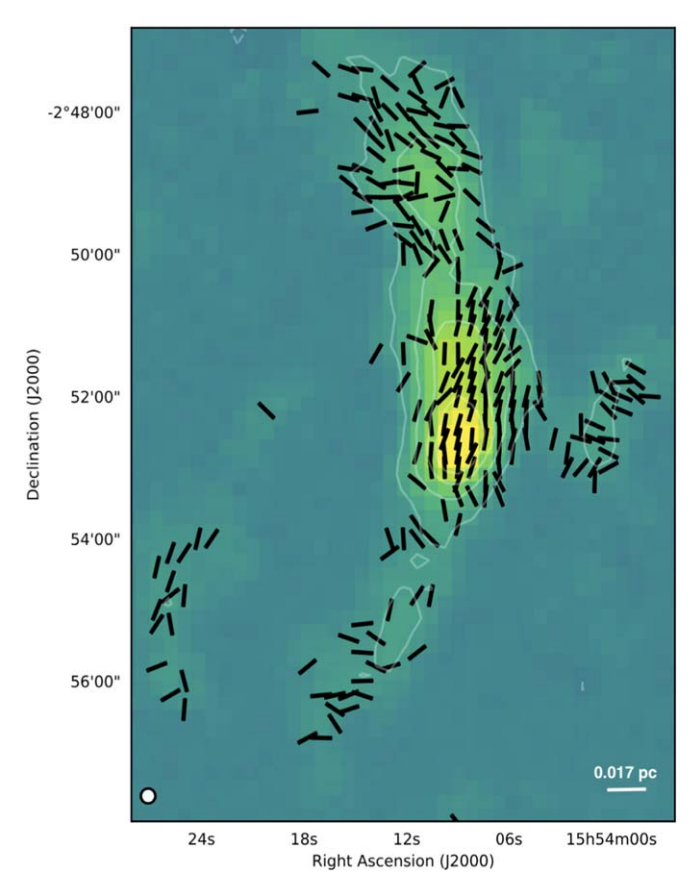


Figure 4. Magnetic field orientations in L183 obtained after rotating the polarization vectors by 90° and shown as normalized line segments independent of the polarization degree P. These vectors correspond to data with $PI/\delta_{PI} > 2$, where PI and δ_{PI} are, respectively, the polarized intensity and its uncertainty. The JCMT beam size at 850 μ m is shown in the lower left corner.

optical depth, μ_{H_2} is the mean molecular weight of the hydrogen gas in the cloud, m_H is the mass of an hydrogen atom, $N_{\rm H_2}$ is the column density, and κ_{ν} is the dust opacity (absorption coefficient). We use a value of 2.8 for μ_{H_2} , and κ_{ν} was calculated for each frequency observed using Equation (10), where β is the emissivity spectral index of the dust, and we assume $\kappa_o = 0.1 \, {\rm cm}^2 \, {\rm g}^{-1}$ and $\nu_o = 10^{12} \, {\rm Hz}$ (Beckwith et al. 1990).

The SED fitting for each pixel was completed in two steps. In the first step, β was left as a free parameter to be fitted simultaneously with the temperature T_d and the column density $N_{\rm H_2}$. In the second step, we instead fixed β to the best-fit value obtained from the first step, before redoing the SED fit to obtain the final values for the temperature and column density. The temperature and column density maps obtained through this procedure for L183 are shown in Figure 7.

The dust temperatures (left panel of Figure 7) in the filament vary approximately between 8.8 and 11 K, with very cold dust present in the two central cores of L183. These results are consistent with those of Ward-Thompson et al. (2002), who found a temperature of 10 ± 3 K in the main, southern, core by fitting a modified blackbody curve to ISOPHOT measurements, as well as with those from Lehtinen et al. (2003), who found a color temperature of 8.3 ± 0.4 K.

The derived column densities (right panel of Figure 7) peak at $\sim 4 \times 10^{22} \, \text{cm}^{-2}$ in the main core. The average column

density in this core is around $3.0 \times 10^{22} \, \mathrm{cm}^{-2}$, which agrees with the average value of $2.7 \times 10^{22} \, \mathrm{cm}^{-2}$ found by Crutcher et al. (2004).

We estimated the hydrogen volume densities $n({\rm H_2})$ of the five regions identified in Figure 5 by assuming they each have a cylindrical geometry, and by adopting the same procedure as Liu et al. (2018). The projected lengths L and radii r of the cylinders for each region of L183, as well as their estimated volume densities and total masses, are given in Table 1.

3.3. Magnetic Field Morphology

Significant amounts of complementary optical and NIR polarization data exist for L183 (Clemens 2012, B.-G. Andersson et al. 2020, in preparation). Panel (a) of Figure 8 shows the optical polarization vectors overlaid on a 100 μ m IRAS map. Panel (b) shows the zoomed-in area of panel (a) with the NIR and submillimeter polarization vectors overlaid on the JCMT 850 μ m dust emission map. Figure 6 shows the distribution of polarization position angles for all of the data sets, optical, NIR, and submillimeter. Because of the 180° ambiguity in polarization position angles we have, for the submillimeter polarization, added 180° to any angle less than 90° in order to make the position angle distribution continuous. Hence, the range in submillimeter wave polarization position angles is 90°–270°.

The optical and NIR polarization data both show single peak distributions averaging around 90°, meaning that the large-scale magnetic field is oriented in the east—west direction (Figure 8). However, the polarization within the core is very different from the large-scale orientation, with a double-peaked distribution instead. We find a distinct peak for the sub-millimeter position angles around 180° with an additional broad distribution centered around 230°. As seen in Figure 8, the former corresponds with the magnetic field in the main core, and is perpendicular to the large-scale field. The broader distribution has a mean of 235° (or 55°), which still differs from the large-scale orientation. Neha et al. (2018) also reported the east—west orientation of B-fields in L183 using *V*-band polarization measurements.

Planck all-sky polarization measurements found interstellar magnetic fields mostly parallel to the diffused low-density regions of the filamentary molecular clouds, whereas field lines tend to be perpendicular in high-density regions (Planck Collaboration et al. 2015, 2016). Several studies on elongated infrared dark clouds have also seen similar features. For instance, Soam et al. (2019) and Liu et al. (2018) have seen changing magnetic fields orientations from the diffuse to dense regions of the G34.43+0.24 and G035.39-00.33 clouds, respectively. It is hard to see a clear change in the magnetic field orientation within the filament containing L183, but it can be noticed that magnetic field lines are following the shape of the filament in diffuse parts such as in regions 1 and 5 (see Figure 5), but not completely parallel to the long axis of filamentary part in region 2, whereas in the dense core (region 3), the magnetic field lines are not perpendicular to the filament either but are instead parallel to it.

3.4. Magnetic Field Strength

The magnetic field strength in each of the regions identified in L183 (see Figure 5) can be calculated with Equation (6). As

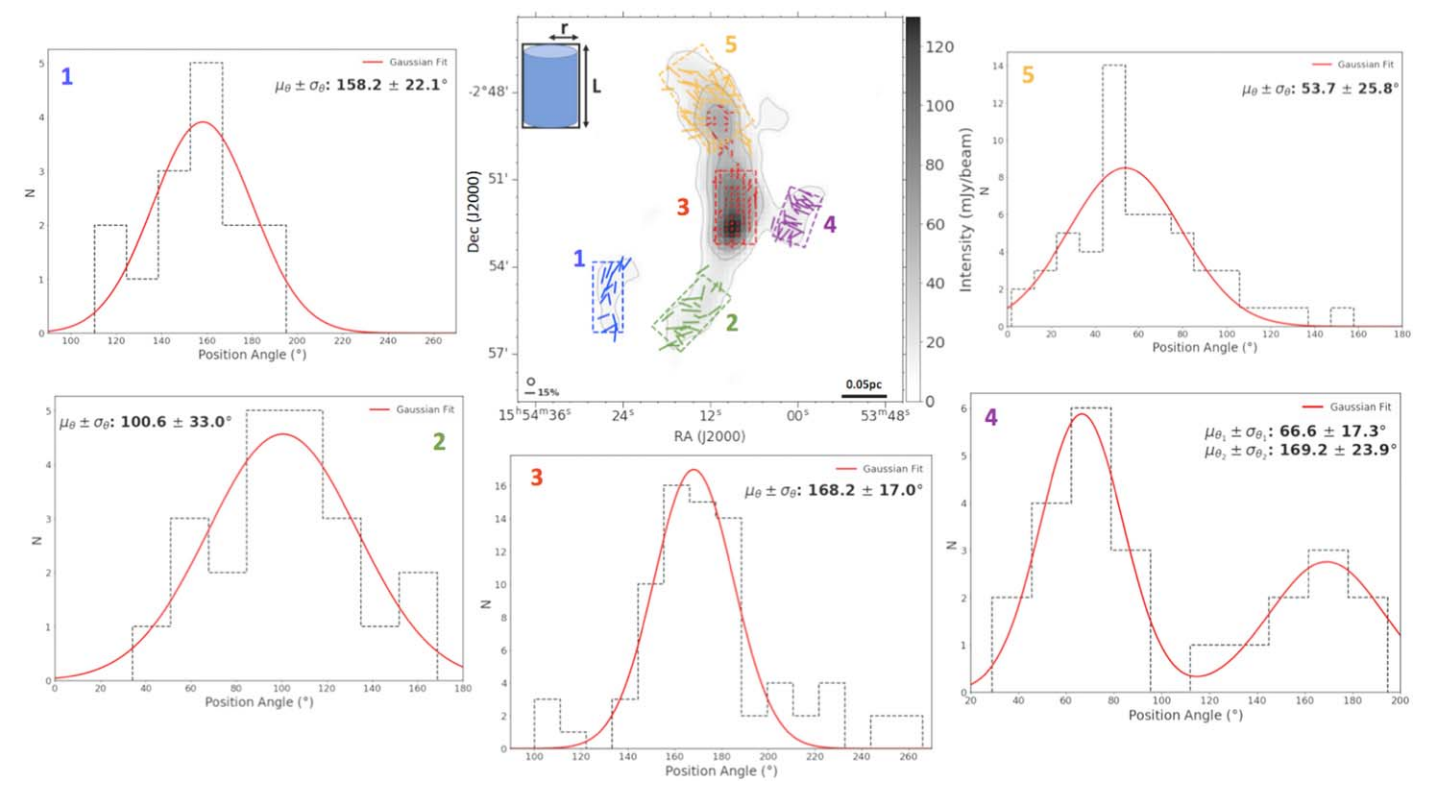


Figure 5. The five regions identified in L183 with their respective distributions of position angles. Each panel includes the mean and standard deviation of the Gaussian fit (red line). The background image is the 850 μ m dust emission map. The scale for the vectors is shown in the bottom left along with JCMT 850 μ m beam size. The red vectors show data with I > 50 mJy beam⁻¹, while all other vectors instead show data where I < 50 mJy beam⁻¹. The regions are drawn as rectangular boxes with dimensions listed in Table 1 as shown by the dust emission map.

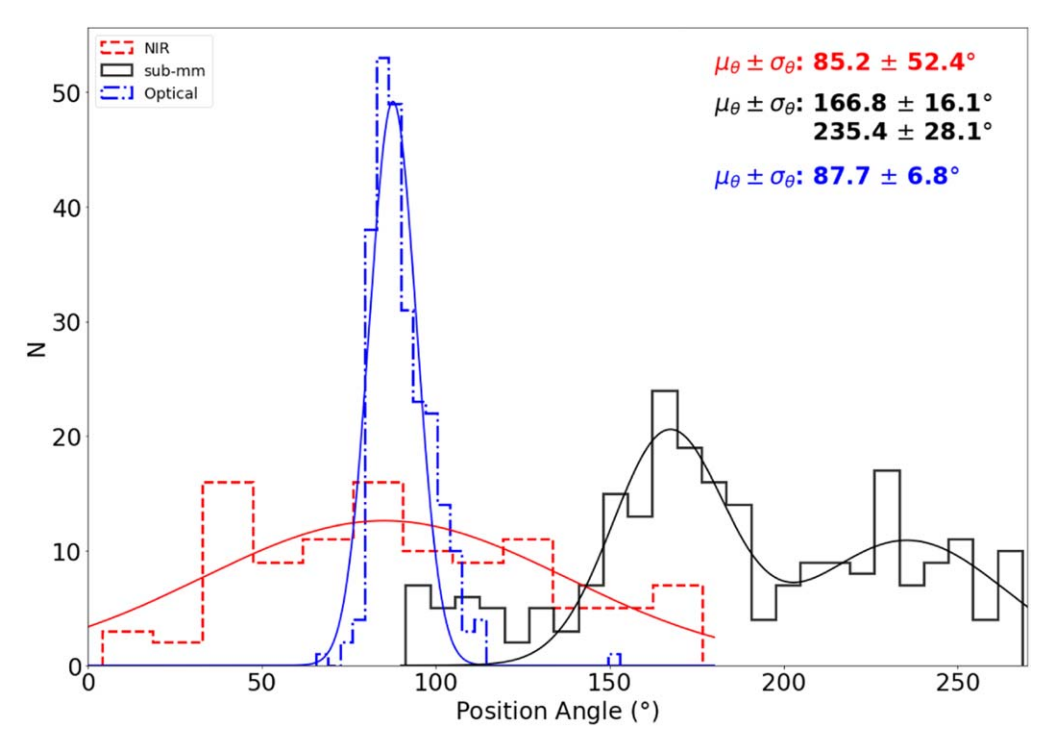
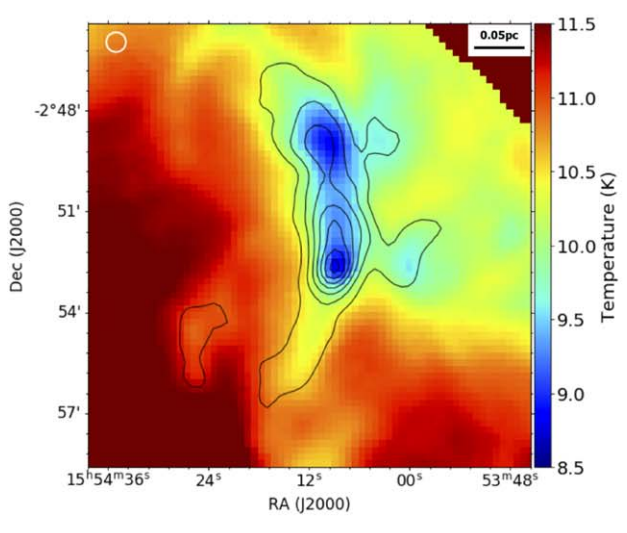


Figure 6. Histogram showing the distributions of magnetic field position angles (POL-2 polarization position angles rotated by 90°). Due to the 180° ambiguity in magnetic field direction, the POL-2 position angles that are less than 90° have been rotated by 180° to best demonstrate the observed double-Gaussian distribution. The POL-2 position angles correspond to data with $PI/\delta PI > 2$.

described in Section 3.2, the volume density for each region can be found in Table 1. Additionally, the values for Δv were taken from N₂H⁺(1-0) measurements by Lee et al. (2001).

Furthermore, we employed a similar method to the one presented by Crutcher et al. (2004) in order to calculate the dispersion of polarization angles σ_{θ} .



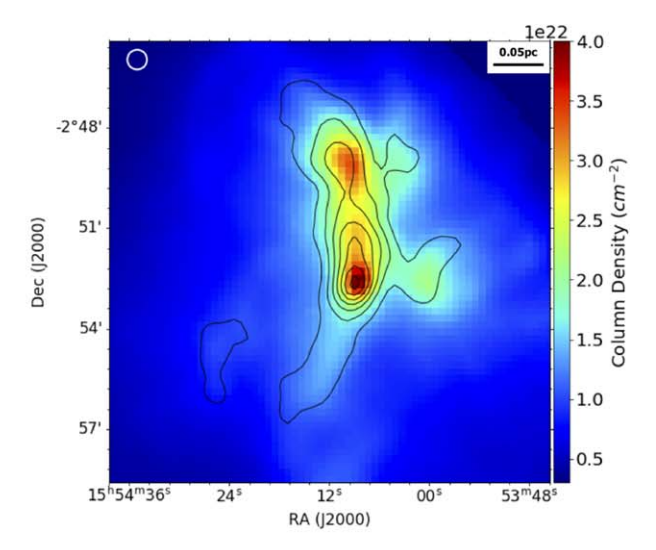


Figure 7. The left panel shows the fitted dust temperature T_d map in L183, and the right panel shows the corresponding column density $N_{\rm H2}$ map. The overlaid contours on both plots are from the SCUBA-2 850 μ m dust emission map. Each map is smoothed to the 35.2" beam size of the Herschel 500 μ m observations, which is shown by the circle in the upper left corner.

Within each region, we measure the difference between the polarization angle at a given position and the mean polarization angle in the region (i.e., $\theta-\theta$), which should probe the random variations of the magnetic field. The distribution of these measured deviations was fitted with a Gaussian function, and we combined the mean of this distribution ($\Delta\theta$) and the angle uncertainties $\delta\theta$ derived from Equation (4) to calculate the dispersion σ_{θ} using the following relation: $\sigma_{\theta} = \sqrt{\delta\theta^2 - \Delta\theta^2}$.

In region 4, there appears to be two distinct populations of vectors (see corresponding histogram in Figure 5), so we found the dispersion σ_{θ} for both populations by splitting them between values less than and greater than 100° . We then took the average dispersion for both populations to calculate the magnetic field strength in that specific region.

Using the previously derived values for $n(H_2)$, Δv , and σ_{θ} summarized in Table 1, we calculated the magnetic field strength in each region using Equation (6). The uncertainties in B_{pos} were calculated using:

$$\frac{\delta B_{\text{pos}}}{B_{\text{pos}}} = \sqrt{\left(\frac{1}{2} \frac{\delta n(H_2)}{n(H_2)}\right)^2 + \left(\frac{\delta \Delta v}{\Delta v}\right)^2},$$
 (11)

where $\delta n(H_2)$ and $\delta \Delta v$ are the uncertainties in volume density and line width, respectively. We calculated the uncertainties in volume density by propagating the uncertainties for the column density. We find magnetic field strengths ranging from ≈ 120 to $\approx 270~\mu\text{G}$, with fractional uncertainties $\delta B_{\text{pos}}/B_{\text{pos}}$ ranging from $\approx 15\%$ to $\approx 24\%$.

3.5. Magnetic Criticality of the Core

The mass-to-flux ratio λ is a unit-less parameter that can be used to quantify the importance of magnetic fields relative to gravity (Crutcher 2004). This parameter can be calculated using the following relation:

$$\lambda = 7.6 \times 10^{-21} \frac{N_{H_2}}{B_{\text{pos}}},\tag{12}$$

where N_{H_2} is the molecular hydrogen column density in cm⁻² and $B_{\rm pos}$ is the plane-of-sky amplitude of the magnetic field strength in μ G. When $\lambda < 1$, then the magnetic field is strong enough to restrain the gravitational collapse of the cloud; this is referred as a "magnetically subcritical" regime. Alternatively, if $\lambda > 1$, then the magnetic field is insufficient by itself to oppose gravity, and the cloud is instead in a "magnetically super-critical" state.

Using our previously derived values for $B_{\rm pos}$ and N_{H_2} (see Table 1), we calculate the mass-to-flux ratios $\lambda_{\rm obs}$ for each region in L183. We note, however, that these ratios can be overestimated due to geometric biases. For this reason, we followed the same procedure as Crutcher (2004), and divided our values of $\lambda_{\rm obs}$ by 3 to obtained the corrected mass-to-flux ratios $\lambda_{\rm cor}$ provided in Table 1. These results indicate that the L183 cloud as a whole is magnetically subcritical.

Based on their survey of molecular lines in starless cores, Lee & Myers (2011) initially found L183 to be a potentially contracting core. However, according to their results (see Figure 10 of Lee & Myers 2011), L183 could also be identified as an oscillating core if the classification criteria are slightly relaxed. Our findings that L183 is magnetically subcritical may therefore help to clarify the dynamical state of this cloud, which was previously unclear using only molecular line data. However, such an expanded analysis is beyond the scope of this paper.

3.6. Energy Budget of the Cloud

The energy budget of a cloud can be estimated by calculating and comparing its thermal $E_{\rm th}$, kinematic $E_{\rm kin}$, magnetic $E_{\rm mag}$, and gravitational $E_{\rm grav}$ energies. First, we define the following relations:

$$E_{\text{mag}} = \frac{B^2 V}{2\mu_a},\tag{13}$$

$$E_{\rm th} = \frac{3M\Delta \nu_{\rm th}^2}{2},\tag{14}$$

Reg	r pc	L pc	$\frac{L}{2r}$	$f(\frac{L}{D})$	$\frac{N_{H_2}}{10^{22} \mathrm{cm}^{-2}}$	$^{n_{H_2}}_{10^5 \text{cm}^{-3}}$	Δv km s ⁻¹	<i>M</i> <i>M</i> _⊙	$\sigma_{ heta}$	$B_{ m pos} \ \mu { m G}$	$\lambda_{ m cor}^{-a}$	J	$\frac{ E_{\rm grav} }{10^{34}}{\rm J}$	$E_{\rm th} \ 10^{34} \ { m J}$	$\frac{E_{\rm mag}}{10^{35}}{\rm J}$	$E_{\rm kin} \\ 10^{35} \rm J$	$\frac{E_{\mathrm{mag}}}{E_{\mathrm{kin}}}$	$J_{ m tot}$
1	0.016	0.081	2.53	1.15876	0.9 ± 0.2	1.2 ± 0.3	0.24 ± 0.03	0.5 ± 0.1	3.7	206 ± 33	0.11 ± 0.03	2.97	7.42 ± 2.97	2.50 ± 0.50	3.2 ± 1.0	1.1 ± 0.5	2.8 ± 0.9	0.17
2	0.021	0.077	1.83	0.98055	1.2 ± 0.3	1.2 ± 0.3	0.35 ± 0.03	0.9 ± 0.2	9.1	123 ± 18	0.25 ± 0.07	4.40	18.3 ± 8.1	4.16 ± 0.92	1.9 ± 0.6	3.6 ± 1.3	0.5 ± 0.2	0.34
3	0.022	0.080	1.82	0.97653	2.8 ± 1.3	2.6 ± 1.2	0.28 ± 0.01	2.2 ± 1.0	4.9	272 ± 64	0.26 ± 0.14	10.70	113 ± 103	10.6 ± 4.8	10.5 ± 5.0	6.2 ± 4.3	1.7 ± 0.8	0.68
4	0.019	0.058	1.53	0.89089	1.8 ± 0.6	2.0 ± 0.6	0.21 ± 0.01	0.9 ± 0.3	6.0	144 ± 24	0.31 ± 0.12	5.42	23.1 ± 15.4	4.25 ± 1.42	1.6 ± 0.5	1.6 ± 0.7	1.0 ± 0.3	0.73
5	0.029	0.102	1.76	0.96039	1.9 ± 0.8	1.3 ± 0.6	0.26 ± 0.01	2.5 ± 1.0	6.6	135 ± 28	0.36 ± 0.17	9.42	113 ± 90	12.0 ± 4.8	5.7 ± 2.4	6.3 ± 3.5	0.9 ± 0.3	0.95

Note. a $\lambda_{\rm cor}$ is the corrected mass-to-flux ratio.

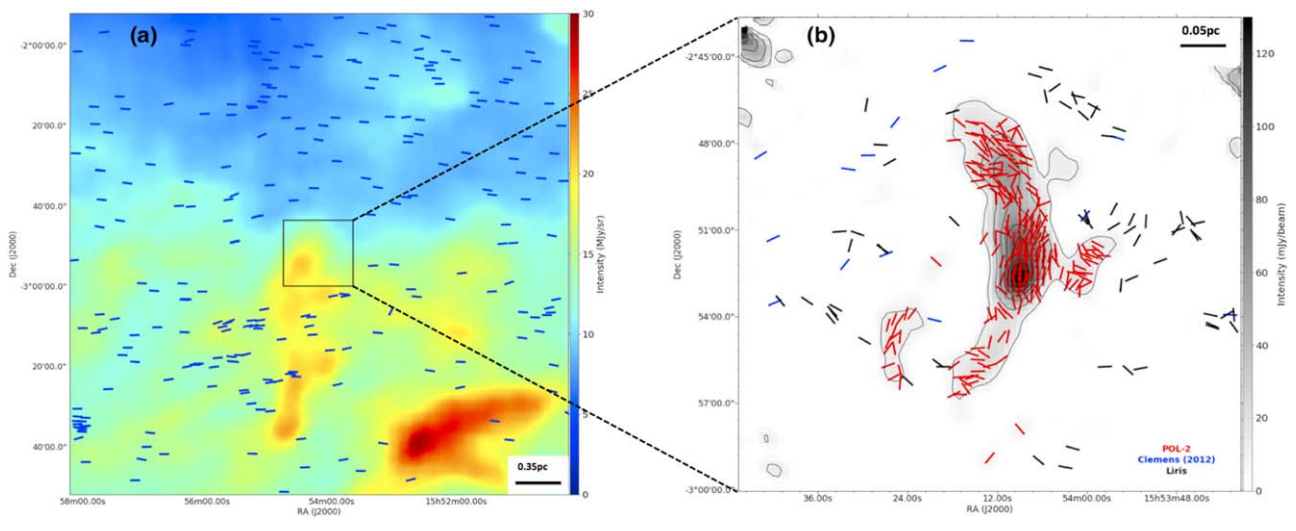


Figure 8. Panel (a): R-band polarization vectors acquired with the 2.1 m telescope at McDonald observatory (B.-G. Andersson & A. Soam et al. 2020, in preparation) plotted on the 100 μ m IRAS emission map. The vector lengths are normalized and do not reflect polarization percentages. The distance scale for the image is shown in the lower right corner. The inset is the location of the L183 cloud observed at 850 μ m by SCUBA-2/POL-2 at the JCMT, and the zoomed-in image is shown in panel (b). Panel (b): H-band polarization measurements from the Long-slit Intermediate Resolution Infrared Spectrograph (LIRIS) at the William Herschel Telescope (B.-G. Andersson & A. Soam et al. 2020, in preparation) are shown in black, while H-band polarimetric data from the Mimir instrument at the Perkins telescope (Clemens 2012) are shown in blue. The 850 μ m polarization observations (this work) are shown with normalized red vectors that have been rotated to show the orientation of the magnetic field, consistent with the optical and NIR vectors. The contours follow the 850 μ m dust emission. The emissions at 100 μ m and 850 μ m microns do not peak at the same location.

$$E_{\rm kin} = \frac{3M\Delta v^2}{2},\tag{15}$$

$$\Delta v = \sqrt{(\Delta v_{\text{turb}})^2 + (\Delta v_{\text{th}})^2}, \qquad (16)$$

and

$$(\Delta v_{\rm th})^2 = v_{\rm sound}^2 = \frac{k_{\rm B} T_{\rm gas}}{\mu_{\rm free} m_H},$$
 (17)

where V is the volume, μ_o is the permeability of free space, $\mu_{\rm free}$ is the mean molecular weight of free particles, Δv is the total FWHM line width from Equation (16), and $\Delta v_{\rm th}$ and $\Delta v_{\rm turb}$ are respectively the contributions of the thermal and turbulent components of this line width. Note that the kinematic energy $E_{\rm kin}$ combines the contribution due to thermal motion of gas particles, as well as the usually stronger energy due to nonthermal supersonic motions from turbulence. The mass M for the region is calculated with $M = n(H_2)m_H \mu_H \pi r^2 L$.

In the previous relations, we assume a mean molecular weight $\mu_{\rm free} = 2.37$ for a gas mixture of H(X = 0.71), He(Y = 0.27), and metals (Z = 0.02), but are neglecting the contribution of metals. Furthermore, we adopt the turbulent line widths $\Delta v_{\rm turb}$ from Lee et al. (2001), and the thermal component $\Delta v_{\rm th}$ was calculated using the measured excitation temperature of 4.6 K from Pagani et al. (2005).

To find out if the five regions we identified in the L183 cloud are gravitationally bound, we also need to compute their gravitational energies. There is no analytical solution for the gravitational potential of finite uniform cylindrical clouds (Kellogg 1929). Nevertheless, a numerical solution can be expressed as a function f(L/D) of the ratio between the length L and the diameter D of the cylinder (Bastien & Mitalas 1979). The values of this function have been tabulated by Bastien (1983) for typical values of L/D from 0.2 to 10.0. If we define

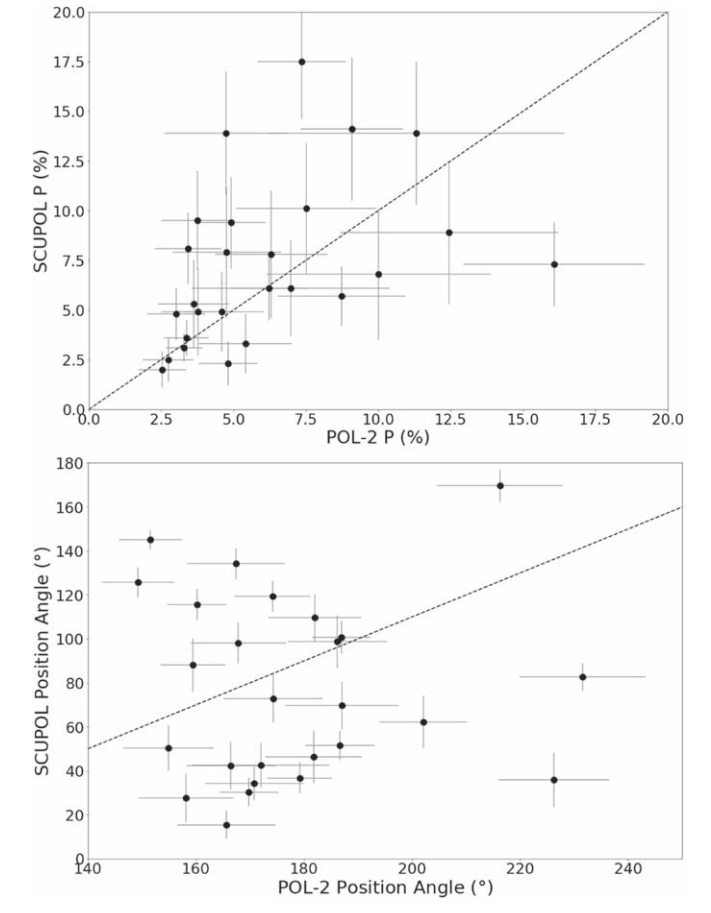


Figure 9. The upper panel shows a comparison between SCUPOL (Matthews et al. 2009) and SCUBA-2/POL-2 (this work) polarization percentages measured toward L183. Similarly, the lower panel shows a comparison of polarization angles. In both plots, the dashed line shows the corresponding one-to-one relation.

a Jeans number, J, one can show that

$$J_{\text{cyl}} = \frac{|E_{\text{grav}}|}{E_{\text{th}}} = \frac{G m}{\frac{k_{\text{B}}T}{\mu_{froe}m_{H}}} f\left(\frac{L}{D}\right), \tag{18}$$

$$J_{\rm cyl} = 3 \frac{m}{m_c} f\left(\frac{L}{D}\right),\tag{19}$$

where m = M/L is the linear mass of the cloud. The critical linear mass for an infinite cylinder is given by

$$m_c = \left(\frac{M}{L}\right)_c = \frac{3k_{\rm B}T}{b\ G\ \mu_{\rm free}m_H}.\tag{20}$$

The constant b depends on the density distribution (i.e., b=1 for uniform density cylinders McCrea 1957), and b=3/2 for equilibrium cylinders (Ostriker 1964). When $m>m_c$, the filament (cylinder) collapses along its axis. Otherwise, if $m< m_c$, the infinite cloud will not collapse, even by increasing the external pressure. The values of f(L/D) for our five regions were determined by a linear interpolation of $\log[f(L/D)]$ between the known values in Table 1 from Bastien (1983). We used Equation (20) with b=1 for uniform density cylinders to get $m_c=7.5M_{\odot}/pc$ assuming a temperature T=4.6~K. Combining Equations (14) and (18), we obtain the gravitational energy $E_{\rm grav}$ of the cylinders, which can be found in Table 1. The value of $E_{\rm grav}$ can be found using equation below.

$$E_{\text{grav}} = -\frac{9}{4} \frac{GM^2}{bL} f(L/D).$$
 (21)

The derived values of the Jeans numbers (=1/ α in many other works) are all > \approx 3.0, and are larger than the critical Jeans numbers for cylinders with 1.5 < L/D < 2.5 which is \approx 0.8 (Bastien 1983). This means that all five regions are gravitationally bound if we consider only gravity and thermal pressure. Moreover, they can accommodate other forces that tend to counter gravity, such as turbulence and magnetic fields.

To take into account other forces, we computed the following quantity:

$$J_{\text{tot}} = \frac{E_{\text{grav}}}{E_{\text{kin}} + E_{\text{mag}}}.$$
 (22)

We see that all the regions in L183, except maybe region 5 (see Figure 5), will not be bound when thermal and nonthermal motions, in addition to magnetic fields, are taken into account. However, we have to be careful since the contribution of a magnetic field depends on its configuration. For example, a toroidal field will constrain the gas on the axis of the filament, and a poloidal field aligned with the axis will increase motions along that axis. In any case, as shown with hydrodynamics calculations, gravity produces significant motions of material along the axis of the filament. After some time, these motions increase the line mass and will make it possible to get sections of the filament to become gravitationally unstable, even if they were originally stable. However, a truly infinite cylindrical cloud will not produce motions along its axis, unless it has density perturbations along its axis.

3.7. Comparison with Previous Polarization Measurements in L183

Matthews et al. (2009) reanalyzed the polarization data previously obtained toward L183 using SCUBA-2/POL-2's predecessor, SCUPOL (Ward-Thompson et al. 2000; Crutcher et al. 2004). They reported 26 data points with $P/\delta P > 2$ toward the main core of L183, while our observations yield 236 such data points in the whole filamentary cloud structure (including the main core). The two data sets are spatially coincident to within 6". In Figure 9, the comparisons between SCUPOL and POL-2 polarization percentages (upper panel) and position angles (lower panel) for L183 are plotted. The degrees of polarization in both samples agree within a 3σ range. We added 180° to the SCUBA-2/POL-2 position angles that are less than 90° to try and find a better relationship between SCUPOL and POL-2 detections. Our data achieve a higher S/N and sensitivity both in the region studied by Matthews et al. (2009) and Crutcher et al. (2004) and in the rest of the large-scale filament, and so the observed differences are likely due to the increased sensitivity of SCUBA-2/POL-2 relative to SCUPOL.

We also compared our results to the magnetic field strength estimates from the SCUPOL data by limiting our DCF analysis to only the region of L183 analyzed by Crutcher et al. (2004). Following their method, we treated the region as a sphere and used the velocity dispersion value of 0.22 km s⁻¹ from Caselli et al. (2002). We obtained $B_{\rm pos} = 105 \pm 24 \,\mu{\rm G}$, consistent with ${\sim}80 \,\mu{\rm G}$ from Crutcher et al. (2004).

4. Summary

- 1. We presented the deepest 850 μ m continuum Stokes I, Q, and U observations to date of the starless cloud L183. The Stokes I map shows an elongated filamentary structure containing two distinct dense cores, as well as several additional, less dense condensations.
- 2. We compared the magnetic field morphology derived from POL-2 data to that of optical and NIR data. We found that, while the large-scale field in the extended cloud run in an east—west direction, the magnetic fields in the cores are predominantly oriented north—south along the direction of the filament's elongation.
- 3. The L183 filamentary structure separates into five subregions for which we performed individual analysis of the polarization degree, as well as of the orientation and strength of the magnetic field. Out of these five regions, region 3, which contains the main core of L183, is found to be the densest ($n_{H_2} = 2.6 \times 10^5 \, \mathrm{cm}^{-3}$) with the strongest magnetic field ($B = 272 \, \mu \mathrm{G}$). All other relatively diffuse regions have similar density and field strengths.
- 4. We estimated the gas column density and the dust temperature of the mapped region by supplementing our 850 μ m data with Herschel SPIRE/PACS continuum observations. The average values of column density and temperature in the filament are $\sim 1.5 \times 10^{22} \, \mathrm{cm}^{-2}$ and $\sim 10 \, \mathrm{K}$, respectively.
- 5. The magnetic field strength in each of the mapped regions ranges from $\sim 120 \pm 18$ to $\sim 270 \pm 64 \,\mu G$. With our derived field strength and column density, we calculated the criticality parameter $\lambda_{\rm cor}$ in these five regions, and found values ranging from 0.1–0.4. These results suggest that the L183 is magnetically subcritical everywhere,

except for region 5, which could be gravitationally bound because of its lower magnetic energy and somewhat larger mass.

We thank the anonymous referee for an encouraging and constructive report, which helped in improving the final manuscript. J.K. is supported by Santa Clara University. A.S. and B-G. A. are supported by NSF Grant-1715876. This research was conducted in part at the SOFIA Science Center, which is operated by the Universities Space Research Association under contract NNA17BF53C with the National Aeronautics and Space Administration. C.W.L. is supported by the Basic Science Research Program through the National Research Foundation of Korea (NRF) funded by the Ministry of Education, Science and Technology (NRF-2019R1A2C1010851). J.E.V. acknowledges financial support from NASA through award # SOF 05-0038 issued by USRA. The JCMT is operated by the East Asian Observatory on behalf of National Astronomical Observatory of Japan; Academia Sinica Institute of Astronomy and Astrophysics; the Korea Astronomy and Space Science Institute; the Operation, Maintenance and Upgrading Fund for Astronomical Telescopes and Facility Instruments, budgeted from the Ministry of Finance of China. SCUBA-2 and POL-2 were built through grants from the Canada Foundation for Innovation. This research used the facilities of the Canadian Astronomy Data Centre operated by the National Research Council of Canada with the support of the Canadian Space Agency.

This research made use of Astropy, ¹¹ a community-developed core Python package for astronomy (Astropy Collaboration et al. 2013; Price-Whelan et al. 2018). The Starlink software (Currie et al. 2014) is currently supported by the East Asian Observatory.

Facilities: JCMT (SCUBA-2, POL-2).

Bastien, P., & Mitalas, R. 1979, MNRAS, 186, 755

Software: Starlink (Currie et al. 2014), Astropy (Astropy Collaboration et al. 2013).

ORCID iDs

Archana Soam https://orcid.org/0000-0002-6386-2906
B-G Andersson https://orcid.org/0000-0001-6717-0686
John E. Vaillancourt https://orcid.org/0000-0001-8916-1828

Chang Won Lee https://orcid.org/0000-0002-3179-6334

References

```
Alves, F. O., Frau, P., Girart, J. M., et al. 2014, A&A, 569, L1 Alves, J. F., Lada, C. J., & Lada, E. A. 2001, Natur, 409, 159 Andersson, B. G., Lazarian, A., & Vaillancourt, J. E. 2015, ARA&A, 53, 501 André, P., Di Francesco, J., Ward-Thompson, D., et al. 2014, in Protostars and Planets VI, ed. H. Beuther et al. (Tucson, AZ: Univ. Arizona Press), 27 Astropy Collaboration, Robitaille, T. P., Tollerud, E. J., et al. 2013, A&A, 558, A33

Bastien, P. 1983, A&A, 119, 109
```

```
Bonnor, W. B. 1956, MNRAS, 116, 351
Caselli, P., Benson, P. J., Myers, P. C., & Tafalla, M. 2002, ApJ, 572, 238
Chandrasekhar, S., & Fermi, E. 1953, ApJ, 118, 113
Chapin, E. L., Berry, D. S., Gibb, A. G., et al. 2013, MNRAS, 430, 2545
Clemens, D. P. 2012, ApJ, 748, 18
Coudé, S., Bastien, P., Houde, M., et al. 2019, ApJ, 877, 88
Crutcher, R. M. 2004, Ap&SS, 292, 225
Crutcher, R. M., Nutter, D. J., Ward-Thompson, D., & Kirk, J. M. 2004, ApJ,
Currie, M. J., Berry, D. S., Jenness, T., et al. 2014, in ASP Conf. Ser. 485,
  Starlink Software in 2013, ed. N. Manset & P. Forshay (San Francisco, CA:
  ASP), 391
Dempsey, J. T., Friberg, P., Jenness, T., et al. 2013, MNRAS, 430, 2534
di Francesco, J., Evans, N. J. I., Caselli, P., et al. 2007, in Protostars and Planets
   V, ed. B. Reipurth, D. Jewitt, & K. Keil (Tucson, AZ: Univ. Arizona
  Press), 17
Ebert, R. 1955, ZAp, 37, 217
Franco, G. A. P. 1989, A&A, 223, 313
Friberg, P., Bastien, P., Berry, D., et al. 2016, Proc. SPIE, 9914, 991403
Hildebrand, R. H., Kirby, L., Dotson, J. L., Houde, M., & Vaillancourt, J. E.
  2009, ApJ, 696, 567
Holland, W. S., Bintley, D., Chapin, E. L., et al. 2013, MNRAS, 430, 2513
Houde, M., Vaillancourt, J. E., Hildebrand, R. H., Chitsazzadeh, S., &
  Kirby, L. 2009, ApJ, 706, 1504
Jones, T. J., Bagley, M., Krejny, M., Andersson, B. G., & Bastien, P. 2015, AJ,
Kauffmann, J., Bertoldi, F., Bourke, T. L., Evans, N. J. I., & Lee, C. W. 2008,
   A&A, 487, 993
Kellogg, O. D. 1929, Foundations of potential theory (Berlin: Springer)
Lee, C. W., & Myers, P. C. 2011, ApJ, 734, 60
Lee, C. W., Myers, P. C., & Plume, R. 2004, ApJS, 153, 523
Lee, C. W., Myers, P. C., & Tafalla, M. 1999, ApJ, 526, 788
Lee, C. W., Myers, P. C., & Tafalla, M. 2001, ApJS, 136, 703
Lehtinen, K., Mattila, K., Lemke, D., et al. 2003, A&A, 398, 571
Liu, T., Li, P. S., Juvela, M., et al. 2018, ApJ, 859, 151
Lynds, B. T. 1962, ApJS, 7, 1
Machida, M. N., Inutsuka, S.-i., & Matsumoto, T. 2008, ApJ, 676, 1088
Matthews, B. C., McPhee, C. A., Fissel, L. M., & Curran, R. L. 2009, ApJS,
McCrea, W. H. 1957, MNRAS, 117, 562
Neha, S., Maheswar, G., Soam, A., & Lee, C. W. 2018, MNRAS, 476, 4442
Ostriker, E. C., Stone, J. M., & Gammie, C. F. 2001, ApJ, 546, 980
Ostriker, J. 1964, ApJ, 140, 1529
Pagani, L., Lagache, G., Bacmann, A., et al. 2003, A&A, 406, L59
Pagani, L., Pardo, J. R., Apponi, A. J., Bacmann, A., & Cabrit, S. 2005, A&A,
  429, 181
Pattle, K., & Fissel, L. 2019, FrASS, 6, 15
Planck Collaboration, Ade, P. A. R., Aghanim, N., et al. 2015, A&A,
  576, A104
Planck Collaboration, Ade, P. A. R., Aghanim, N., et al. 2016, A&A,
  586, A138
Price-Whelan, A. M., Sipőcz, B. M., Günther, H. M., et al. 2018, AJ, 156, 123
Soam, A., Liu, T., Andersson, B. G., et al. 2019, ApJ, 883, 95
Tafalla, M. 2005a, in IAU Symp. 231, Astrochemistry: Recent Successes and
  Current Challenges, ed. D. C. Lis, G. A. Blake, & E. Herbst (Cambridge:
  Cambridge Univ. Press), 17
Tafalla, M. 2005b, ASSL, 324, 31
Wang, J.-W., Lai, S.-P., Eswaraiah, C., et al. 2019, ApJ, 876, 42
Wardle, J. F. C., & Kronberg, P. P. 1974, ApJ, 194, 249
Ward-Thompson, D., André, P., & Kirk, J. M. 2002, MNRAS, 329, 257
Ward-Thompson, D., Kirk, J. M., Crutcher, R. M., et al. 2000, ApJL,
  537, L135
```

Beckwith, S. V. W., Sargent, A. I., Chini, R. S., & Guesten, R. 1990, AJ,

99, 924

¹¹ http://www.astropy.org